Received: 01 July 2025 | Revised: 14 November 2025 | Accepted: 16 November 2025

DOI: 10.5185/amlett.2026.011780

OPEN ACCESS

RESEARCH

Dielectric Studies on Dendrite-shaped PbTe, Rod-shaped SnTe and their Nanocomposite

P. Indra Devi[1]*, R. Karunamoorthi[2], M. Sivabharathy[3] and K. Ramachandran[2]

[1]Department of Physics,
Sri Meenakshi Govt. Arts College for Women, Madurai 625002, India

[2]School of Physics,
Madurai Kamaraj University,
Madurai – 625 021, Tamilnadu, India

[3]Department of Physics,
Sethu Institute of Technology,
Virudhunagar - 626 115, Tamilnadu, India

***Corresponding author:**
E-mail: indradevi01@gmail.com

ABSTRACT

Dendrite shaped PbTe, SnTe nanorods and their nanocomposites were successfully synthesized via a simple hydrothermal method using hydrazine hydrate as a reducing agent. The formation of nanostructures was confirmed by high resolution transmission electron microscopy (HRTEM) in both the samples. A detailed study on dielectric properties of these samples in the frequency range of 50 Hz–50 MHz at various temperatures (50-100 °C) shows a tremendous enhancement in PbTe and SnTe nanostructures compared to bulk. But in the case of composite system PbTe: SnTe have significantly lower dielectric constants than pure samples due to no additional percolation threshold in the system.

KEYWORDS

Dendrite shape, Hydrothermal, Dielectric properties, Percolation threshold.

INTRODUCTION

In recent years, IV-VI semiconductors characterized by well-defined nano-micro dependent structures, such as PbTe and SnTe, have emerged as a crucial element in contemporary electronic tool technology [**1-3**]. This has led to extensive theoretical and experimental studies due to their unique physical properties, including high carrier mobilities, elevated dielectric constants, and narrow band gaps [**4**]. The investigation of the PbTe–SnTe system has garnered significant attention owing to its numerous intriguing features when compared to III–V or II–VI semiconductors. The primary characteristics include the inversion of valence and conduction band symmetry between PbTe and SnTe, which theoretically results in a zero-gap compound for Sn compositions around 35%, thereby influencing the high carrier mobilities [**5**]. They are distinctive among polar compounds and have vital applications in infrared detectors, light-emitting devices, and thermoelectric devices [**6**]. One remarkable attribute of IV-VI semiconductors is their ability to transition to quantum confinement at relatively large particle sizes due to the high value of the Bohr excitation radius (50 nm for PbTe and 46 nm for SnTe) [**7,8**]. Furthermore, this system exhibits an unusually high value of static dielectric constant (~ 103 at 4.2 K for PbTe and ~ 380 for SnTe) [**9**], which facilitates a high degree of electron localization and minimizes random potential fluctuations within the nanostructures. Recently, numerous researchers have fabricated various morphologies of PbTe and SnTe nanostructures, including dendrite-shaped [**10**] and sponge-like structures [**11**]. However, our intention here is to synthesize dendrite-shaped PbTe and rod-shaped SnTe using a straightforward hydrothermal method for dielectric studies. Recently, Li *et al.* [**12**] synthesized dendrite-shaped PbTe through electrochemical deposition without templates for thermal properties. Additionally, Zhu *et al.* [**13**] reported on complex PbTe hopper crystals with high hierarchy via the hydrothermal approach. In a similar vein, Schlecht *et al.* [**14**] synthesized SnTe nanorods using a reflux method. However, there remains a significant gap in understanding the dielectric properties in connection with nanostructures, which have a substantial impact on device performance. This study specifically emphasizes the investigation of dielectric properties of IV-VI semi-conductors' nanostructures. To the best of our knowledge there is no experimental reports are available on the dielectric properties of dendrite shaped PbTe, SnTe, and their nanocomposites. Since both are exhibit excellent piezoelectric and ferroelectric substances, an effort is made to study the dielectric properties of these materials, and the enhancement of dielectric properties are addressed with percolation theory herein.

EXPERIMENT

PbTe, SnTe, and their nanocomposites were synthesized using a simple hydrothermal method as described by Poudel *et al.* [**10**]. In the standard procedure for synthesizing PbTe dendrites, 200 µM of PEG and 1.5 M of NaOH were introduced into 50 mL of de-ionized water. After a brief stirring period, 0.05 M each of sodium tellurite and lead acetate (PbAc. $3H_2O$) were incorporated into the solution and mixed thoroughly. Subsequently, 15 mL of hydrazine hydrate was added, and the mixture was transferred into a Teflon-lined autoclave, where it was maintained at 150°C for 24 hours. For SnTe synthesis, a similar method was employed, substituting PbAc.$3H_2O$ with $SnCl_2$. $2H_2O$ as the source of Sn. The PbTe:SnTe nanocomposite was produced by adding varying amounts of $SnCl_2$. $2H_2O$ (10, 20, and 30 at.%) to the PbTe stock solution. The resulting precipitate was subjected to centrifugation, washed multiple times with de-ionized water and acetone, and subsequently dried in air at room temperature to yield the powder. The samples synthesized are designated as Z1 (PbTe), Z2 (SnTe), and Z3 (PbTe:SnTe). A typical flowchart illustrating the preparation process for the PbTe, SnTe, and PbTe:SnTe nanocomposite is presented in **Fig. 1**.

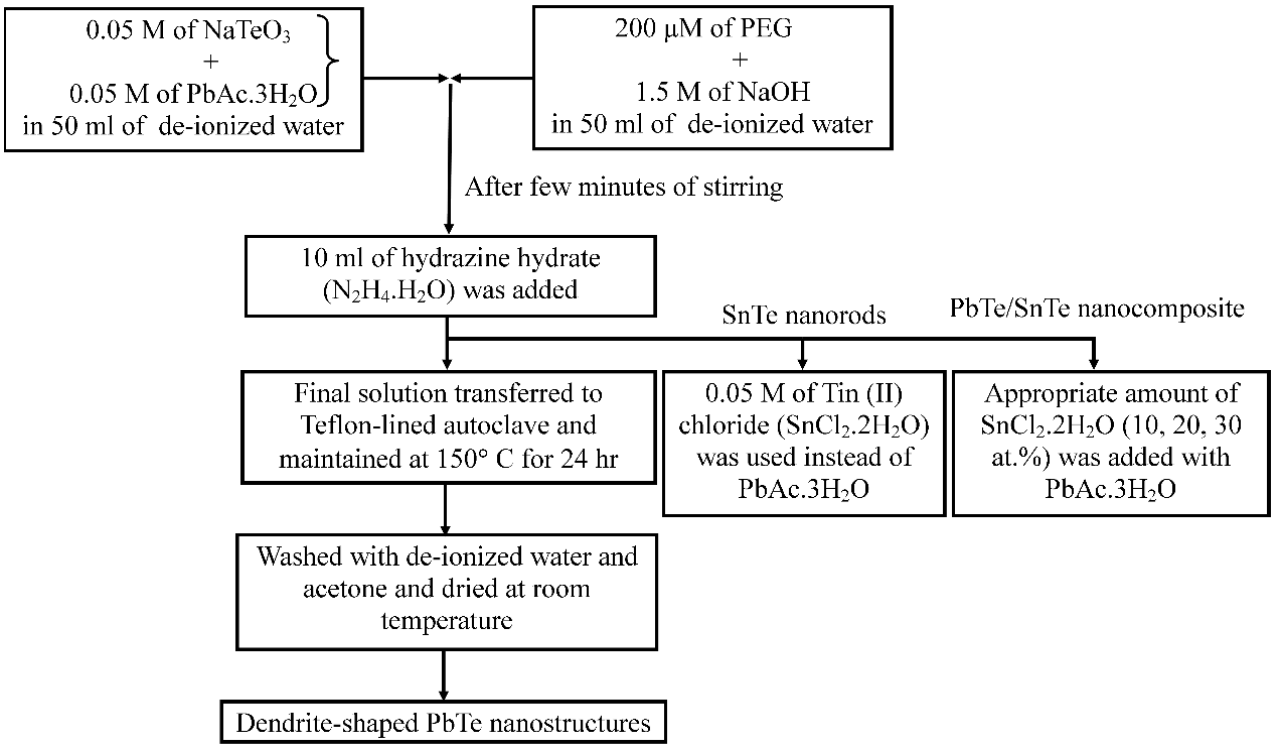

Fig. 1. Flowchart for the preparation of PbTe, SnTe and PbTe/SnTe nanocomposite.

RESULTS AND DISCUSSION

XRD Analysis

The structural analysis of the synthesized Z1, Z2, and Z3 samples was conducted by recording the X-ray diffraction (XRD) spectrum at room temperature using an X-ray diffractometer (PANalytical X'Pert). The spectrum was captured in the 2θ range of 10 to 90° with a step size of 0.02° utilizing Cu-Kα radiation (wavelength 1.54056Å). **Fig. 2 (A)** illustrates the XRD spectra of the Z1 sample, which displays prominent diffraction peaks at (200), (220), and (222), indicating the cubic structure of PbTe, in accordance with JCPDS data (Card No: 65-8350). The lattice parameters of pure PbTe were determined to be a = 6.33 Å. Similarly, for SnTe, the indexed diffraction peaks align well with the cubic structure of SnTe as per JCPDS data (Card No: 65-7162), with a lattice parameter of a = 6.30 Å. Additionally, some Te peaks were observed due to unreacted Te precursors alongside the SnTe diffraction peaks. The XRD spectra of the nanocomposite did not reveal any new diffraction peaks corresponding to SnTe, as the dominant diffraction peaks of PbTe and SnTe exhibit nearly identical two theta values, preventing the identification of new peaks in the composite materials. However, the magnified image (**Fig. 2(B)**) distinctly shows that the dominant peak shifts towards SnTe, confirming the presence of SnTe within the PbTe matrix. As the concentration of Sn increases, the intensity of the XRD peak decreases while the FWHM increases, which corroborates the morphological transition within the composite system.

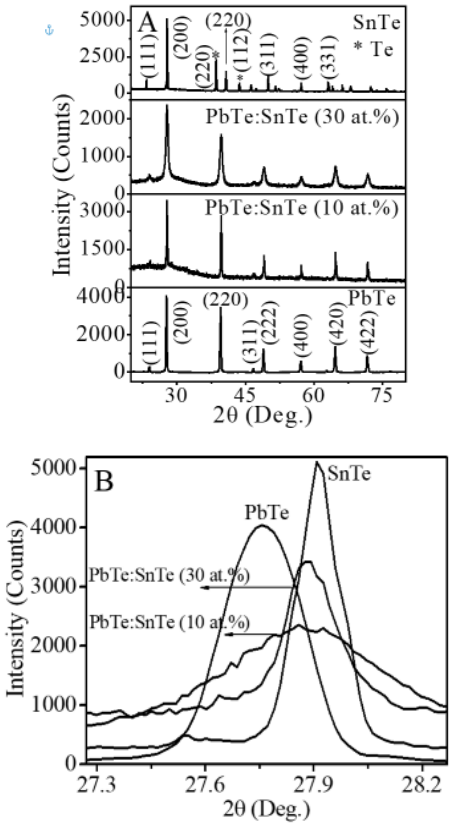

Fig. 2. (A) XRD spectra of Z1, Z2 and Z3 samples (B) Magnified image of XRD spectra.

SEM Analysis

The surface morphology of the samples was examined using scanning electron microscopy (Hitachi S-3400N, Japan). **Fig. 3(a)** illustrates that PbTe (Z1) exhibits a dendritic morphology. The growth mechanism of PbTe dendrites can be described as follows: due to the cubic symmetry of PbTe, they tend to develop into a cubic shape once a particle reaches a certain minimum size in the absence of constraints; these cubic particles can serve as nucleation sites for the formation of a secondary layer from their corners. The secondary layer can initiate growth solely from the corners of the cubic nuclei, where the concentration of the surfactant (PEG – surfactant) is lower and the surface energy is higher compared to the faces. Growth will not occur at the center of the face, where the surfactant concentration is elevated, thus preventing particles from diffusing through. This process persists until the reaction ceases. **Fig. 3(b)** depicts the formation of rod-shaped pure SnTe (Z2). Likewise, **Fig. 3(c)** and **Fig. 3(d)** present the SEM images of nanocomposite PbTe/SnTe (10 at. %) and PbTe/SnTe (30 at. %), respectively. In the composite system, the morphology of the samples is influenced by the increase in Sn content, although their structure remains unchanged. The XRD results have already clearly indicated the morphological transition of PbTe with the increase in Sn content, which is further corroborated by SEM analysis.

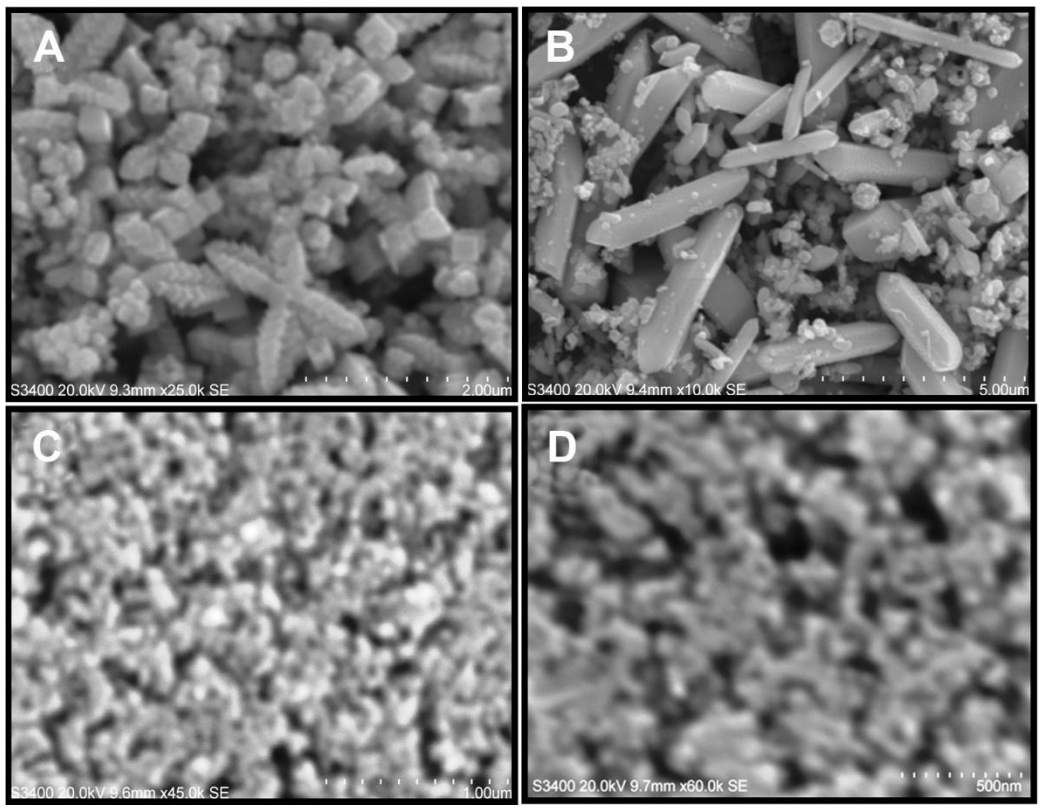

Fig. 3. SEM images of (A) Z1 (B) Z2 (C) Z3 (10 at.% of Sn) (D) Z3 (30 at.% of Sn) samples.

TEM Analysis

Additionally, we verified the development of nanostructures in the Z1 and Z2 samples through TEM analysis, as illustrated in **Fig. 4**. **Figs. 4 (A,B)** and C depict the dendrite-shaped PbTe with a diameter of 10 µm. **Fig. 4D** presents the selected area electron diffraction (SAED) pattern of the Z1 sample, which indicates a single-crystalline structure with excellent crystallinity, aligning with the XRD results. Recently, Wan *et. al.* [**5**] synthesized PbTe nanorods with diameters ranging from 10 to 50 µm [**15**]. **Figs. 4E, F** and G display typical TEM images of SnTe nanorods, measuring 150 µm in length and 50 µm in diameter. A representative HRTEM image **(Fig. 4G)** reveals a lattice spacing of approximately 3.183 Å, which is comparable to the (200) lattice spacing of rock salt SnTe, suggesting that the rod growth is preferentially oriented in the (200) direction. The SAED pattern **(Fig. 4H)** of the Z2 sample also confirms its single crystalline nature.

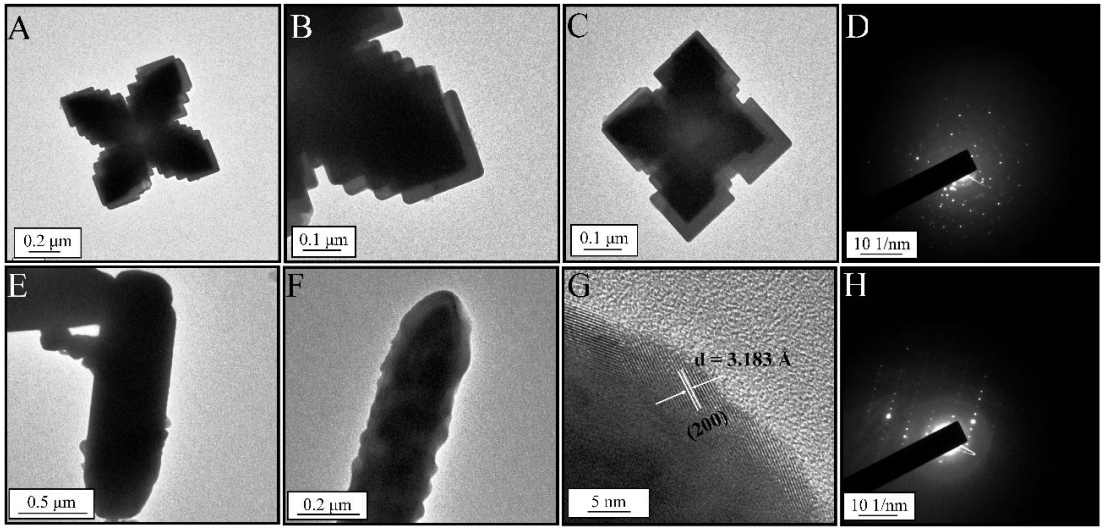

Fig. 4. HRTEM images of (A, B and C) dendrite shaped PbTe (D) SAED pattern of Z1 and (E, F and G) SnTe nanorods (H) SAED pattern of Z2.

EDS Analysis

The elemental compositions of the samples were analyzed using energy dispersive analysis of X-ray (EDAX) (Nortan System Six, Thermo Electron Corporation Instrument Super DRYII, USA). Figure 5 illustrates the EDS spectra for the Z1 and Z3 (10 at.% of Sn) samples. Table 1 presents the atomic percentages of Pb, Te, and Sn for both pure and PbTe/SnTe nanocomposites. The Z1 sample indicates the presence of only Pb and Te elements, thereby confirming the absence of any other impurities. The atomic percentages of Pb and Te in the samples are 60.8 and 39.2, respectively. In the PbTe: SnTe (10 at.%) nanocomposite, the atomic percentages of Pb, Te, and Sn were found to be 59.8, 38.8, and 1.4, respectively. Although we intended to add 10 at.% of SnTe to the composite system, only 1.4 at.% of Sn was incorporated, with the remainder being washed away during the synthesis process. Essentially, both PbTe and SnTe represent complex systems, making their composite formation challenging.

Table 1. The chemical composition of Z1 and Z3 (10 at.% of Sn) samples.

Sample	Pb (at. %)	Te (at. %)	Sn (at. %)
PbTe (Z1)	60.8	39.2	--
PbTe: SnTe (10 at.%) (Z3)	**59.8**	**38.8**	**1.4**

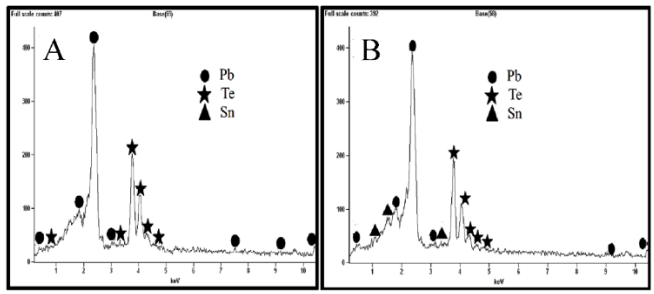

Fig. 5. EDS spectra of Z1 and Z3 (10 at.% of Sn) samples.

Raman Analysis

Raman measurements were carried out using the Renishaw InVia laser Raman microscope equipped with a He-Ne laser (633 nm). The Raman spectra of PbTe reveal (**Fig. 6**) modes at 117, 137, 259, and 743 cm^{-1}. The peaks at 117 and 137 cm^{-1} may be linked to Te-like phonon modes. Similar telluride peaks were reported by Romcevic *et al.* [**15**] and Larramendi *et al.* [**16**]. These Te-related bands are also present in SnTe and PbTe: SnTe samples. The peaks at 259 and 743 cm^{-1} correspond to the Pb peak. The Raman spectra of SnTe display a prominent peak around 681 cm^{-1}, which aligns with the symmetric Sn–O stretching. The vibrational modes in both PbTe and SnTe show a slight red shift when compared to the bulk system [**17**]. In the case of the nanocomposite, a dominant Raman mode was identified at

693 cm^{-1}, alongside Te and Pb peaks. All peaks in the composite system exhibit a slight blue shift relative to the pure samples. The Raman spectroscopic findings confirm the presence of Sn in the composite system.

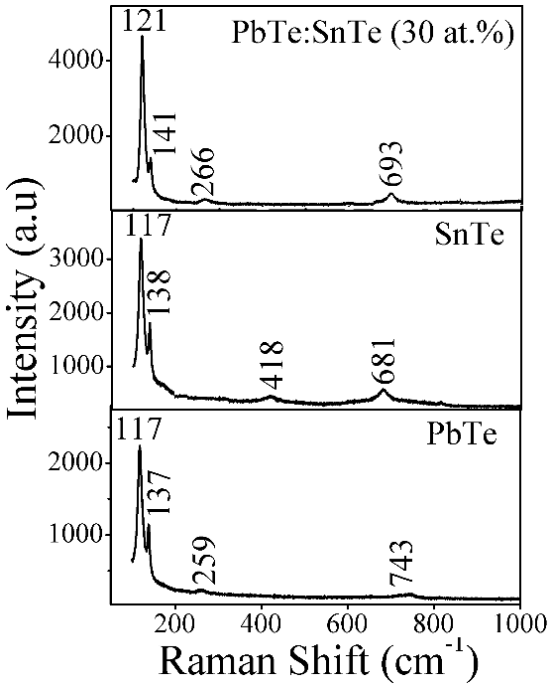

Fig. 6. Raman spectra of Z1, Z2 and Z3 (30 at.% of Sn) samples.

Dielectric studies

The dielectric studies of Z1, Z2 and Z3 samples were carried out by an impedance analyzer (model: PSM1735-Numetriq) in the frequency range of 50 Hz-50 MHz at various temperature (50-100°C) is shown in **Fig.7**. Dielectric constant or relative permittivity is calculated from

$$\varepsilon_r = \frac{C(\omega)d}{\varepsilon_0 A} \quad (1)$$

where d is the sample thickness and A is the surface area of the sample ε_0 is the free space permittivity (8.854×10^{-14} F cm^{-1}). **Fig. 7 (A, B & C)** illustrates the variation of relative dielectric permittivity (ε) as a function of frequency. It has been observed that the relative dielectric permittivity diminishes with an increase in frequency, which signifies the typical dielectric dispersion. At elevated frequencies, the dielectric constant remains unaffected by frequency due to the incapacity of electric dipoles to keep pace with the rapid fluctuations of the alternating applied electric field, a behavior commonly seen in most dielectric materials [**18**]. Likewise, the high value of dielectric constant at low frequencies is primarily attributed to the presence of space charge [**19**].

Conversely, the dielectric permittivity of dendrite-shaped (Z1) PbTe demonstrates (**Fig. 7.A**) a remarkable enhancement when compared to bulk PbTe (Bulk PbTe ~1000) [**5**]. For clarity, dendrite-shaped PbTe exhibits a dielectric permittivity of approximately ~17825 at 50 Hz (100°C). In comparison to bulk PbTe, dendrite-shaped PbTe shows a significantly greater dielectric permittivity, nearly 17 times higher, which can be explained by the low percolation threshold. A similar enhancement in dielectric properties was reported by Wang *et al.* [**20**], who noted that the dielectric constant of PVDF/ZnO-nanorods is ten times greater than that of PVDF/ZnO nanoparticles. They asserted that nanoparticles lacking any distinctive morphology do not significantly enhance the dielectric constants due to the absence of a percolation threshold. In contrast, special morphologies exhibit a low percolation threshold. Similarly, SnTe nanorods demonstrate an enhancement in dielectric permittivity of approximately ~9943 at 50 Hz (100 °C) compared to bulk SnTe (~380). However, in the composite, the dielectric permittivity experiences a significant reduction (~885 at 50 Hz) due to surface morphology. The SEM image (**Fig. 3 C & D**) of Z3 clearly illustrates the affected morphology. Nanoparticles lacking any distinctive morphology do not significantly enhance the dielectric constants because no percolation threshold exists in this case. In contrast, special morphologies exhibit a low percolation threshold.

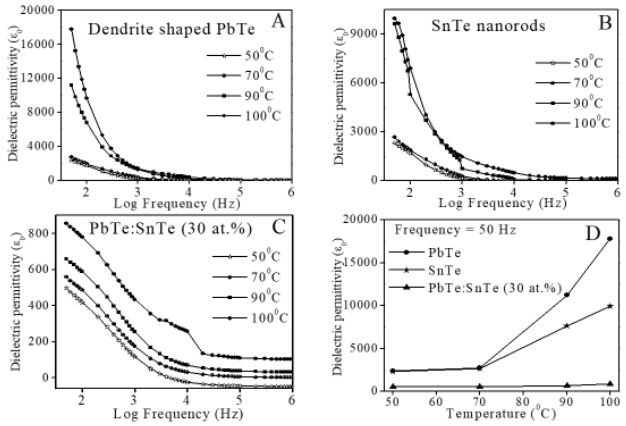

Fig. 7. (A, B and C Frequency dependent and (D) temperature dependent dielectric permittivity of Z1, Z2 and Z3 samples.

CONCULSION

This document presents a straightforward hydrothermal method for the large-scale production of dendrite-shaped PbTe and rod-shaped SnTe nanostructures. X-ray diffraction (XRD), high-resolution transmission electron microscopy (HRTEM), and selected area electron diffraction (SAED) analyses reveal that both PbTe and SnTe exhibit a cubic structure with excellent crystallinity. Morphological examinations through scanning electron microscopy (SEM) and transmission electron microscopy (TEM) demonstrated the successful formation of dendrite-shaped PbTe and rod-shaped SnTe, respectively. Additionally, the potential mechanism behind the

formation of dendrite-shaped PbTe is discussed. Raman spectroscopy further validated the presence of Sn within the PbTe system. The synthesized PbTe and SnTe nanostructures are capable of significantly enhancing the dielectric constant compared to their bulk counterparts, making them suitable for capacitor applications.

ACKNOWLEDGEMENTS

We are thankful to UGC-DRS, UPE & RFSMS for financial support.

REFERENCES

1. Kai Chang; John,W. D.;Villanova; Jing-Rong Ji ; Souvik Das ; Felix Küster; Salvador Barraza Lopez; Paolo Sessi; Stuart S.P Parkin, *Adv. Mater.*, **2021**, 33, e2102267.
2. Song, W.; Cao,W.; Zhao, W.; Ding, J. *J. Condens. Matter Phys.,* **2023**,35, 355001.
3. Azab, A.A.; Azza, A.; Ward, G.M.; Mahmoud Eman.; M El-Hanafy; El-Zahed, H.; Terra, F.S. *J. Semicond.,* **2018**, 39, 123006.
4. Kungumadevi, L.; Sathyamoorthy, R.; Subbarayan, A. *Solid-State Electron.,* **2010**, 54, 58.
5. Wang, Z. L.; Song, J. H. *Science*, **2006**, 312, 242.
6. Ferreira, S. O.; Abramof, E.; Rappl, P. H. O.; Ueta, A. Y.; Closs, H.; Boschetti, C. *J. Appl. Phys*., **1998,** 84, 3650.
7. Kungumadevi, L.; Rajasekar, K.; Subbarayan, A.; Sathyamoorthy, R. *Ionics,***2008,** 14, 63.
8. Barraza-Lopez, S.; Fregoso, B. M.; Villanova, J. W.; Parkin, S. S. P.; Chang, K. *Rev. Mod. Phys.,***2021**, 93, 011001.
9. Grabecki, G.; Wrobel, J.; Dietl, T.; Janik, K. E.; Aleszkiewicz, M.; Papis, E.; Kaminska, E.; Piotrowska, A.; Springholz, G.; Bauer, G. Phys. *Rev. B.,* **2005**, 72, 125332.
10. Poudel, B.; Wang, W. Z.; Wang, D. Z.; Huang, J. Y.; Ren, Z. F. *Journal of Nanoscience and Nanotechnology,* **2005,** 16, 1935.
11. Villanova, J. W.; Kumar, P.; Barraza-Lopez, S. *Phys. Rev. B.,* **2020,** 101, 184101.
12. Guo, H.; Jiang, W.; Fan, H.; He, X.; Li, Y.; Tian, X. *Physica B*, **2020,** 583, 412047.
13. Zhu, J. P.; Yu, S. H.; He, Z. B.; Jiang, J.; Chen, K.; Zhou, X. Y. *Chemical Communications,* **2005,** 5802.
14. Schlecht S Budde, M.; Kienle, L. *Inorg. Chem.,* **2001**, 40, 5719.
15. Romcevic, N.; Trajic, J.; Hadzic, B.; Romcevic, M.; Stojanovic, D.; Lazarevic, Z.; Kuznetsova, T. A.; Khokhlov, D. R.; Rudolf, R.; Anzel, I. *Acta Phys. Pol. A.,* **2009,** 115, 805.
16. Larramendi, E. M.; Berth, G.; Wiedemeier, V.; Husch, K. P.; Zrenner, A.; Woggon, U.; Tschumak, E.; Lischka, K.; Schikora, D. *Semicond. Sci. Technol.*, **2010,** 25, 075003.
17. Brillson, L.; Burstein, E. *Phys Rev Lett.,* **1971**, 27, 317.
18. Kambale, R. C.; Shaikh, P. A.; Bhosale, C. H.; Rajpure, K. Y.; Kolekar, D. *Smart Mater. Struct.*, **2009,** 18, 085014.
19. Somashkhara udupa, K.; Mohan Rao, P.; Sriramana AithalBha, A. P. T.; Avasthi, D. K.*Bull. Mater. Sci.*, **1997**, 20, 1069.
20. Wang, B., Deng, Y.; Xiang, Y.; Guo, L. *Advanced Functional Materials,* **2008,** 18, 2584.
21. Abdulin, Kh. A.; Demin, V. N.; Lebedev, A. I. *Soviet Physics Solid State*, **1986,** 28,1020.
22. Wan, B.; Hu, C.; Liu, H.; Xiong, Y.; Li, F.; Xi, Y.; He, X. *Mater. Res. Bull.*, **2009,** 44,1846.